Structure and evolution of quasi-solid-state hybrid electrolytes formed inside electrochemical cells

Nyalaliska W. Utomo[1], Yue Deng[2], Qing Zhao[1], Xiaotun Liu[1], and Lynden A. Archer[1,2*]

[1]Robert Frederick School of Chemical and Biomolecular Engineering, Cornell University, Ithaca, NY, USA

[2]Department of Materials Science and Engineering, Ithaca, NY, USA

Corresponding Author

Lynden A. Archer

*E-mail: laa25@cornell.edu

Abstract

Solid-state electrolytes (SSEs) formed inside an electrochemical cell by Lewis Acid salt-initiated polymerization of a liquid precursor provide a promising strategy for overcoming problems with electrolyte wetting and access to active electrode components in solid-state batteries. Hybrid solid-state polymer electrolytes (HSPEs) created by in-situ polymerization of a conventional liquid precursor containing electrochemically inert nanostructures that are well-dispersed in the SSE are of particular interest because they offer a mechanism for selectively reinforcing or adding functionality to the electrolyte in all components of an electrochemical cell — removing the need for high degrees of polymerization and long formation times to achieve desirable electrolyte properties. We report on the synthesis, structure, chemical kinetics, and electrochemical characteristics of HSPEs created by $Al(OTf)_3$-initiated polymerization of 1,3-dioxolane (DOL) containing hairy, nano-sized SiO_2 particles. Small-angle x-ray scattering analysis reveals the particles are well-dispersed in DOL. Polymerization kinetics are observed through time-dependent

mechanical property measurements, which reveal altered macrokinetics of ring-opening reaction upon addition of hairy nanoparticles (HNPs). Strong interaction between poly(ethylene glycol) (PEG) molecules tethered to the SiO_2 particles and poly(DOL) lead to co-crystallization — anchoring the nanoparticles in their host. It also enables polymerization-depolymerization processes in DOL to be studied and controlled. To demonstrate the utility of the in-situ formed HSPE, we first create Li|HSPE|Cu electrochemical half cells in which the HSPE is formed by ring-opening polymerization of DOL in the presence of HNPs, $LiNO_3$, and LiTFSI. These cells manifest Coulombic efficiencies (CE) values approaching 99% and stable long-term cycling. As a final proof of concept, we create solid-state Lithium-Sulfur full-cell batteries, which utilize a sulfur-polyacrylonitrile (SPAN) composite material as cathode. The in-situ formed Li|HSPE|SPAN cells show good cycling stability and thus provide a promising path towards all-solid-state batteries created by in-situ formation of mechanically strong SPEs.

Main text begins:

Solid-state rechargeable batteries have in recent years drawn significant attention from researchers, as well as from investors —globally. An important aspect of their promise is that such batteries remove fundamental safety and performance barriers to high-energy, low-cost storage of electrical energy in cells that employ Li metal as anode.[1-3] Limited choices of electrolyte materials able to simultaneously meet the mechanical and electrochemical requirements of such cells slowed early progress towards cost-competitive, practical solid-state batteries by at least three decades.[3] This progress has noticeably quickened over the last decade as a number of solid-state electrolyte options, including inorganic solids (*e.g.* ceramics), organic polymers, and organic-inorganic hybrids, have emerged.[3] Solid state electrolytes (SSEs) based on inorganic glasses are conventionally thought to be attractive because they provide enhanced safety due to their non-volatile nature, slower chemical reactions with the metallic Li electrode, as well as for their fundamental ability to mechanically retard non-planar/dendritic growth of the Li anode during repeated cycles of charge and discharge.[4,5] While significant progress in synthesis and fabrication of versions of these materials with high room-temperature ionic conductivity and good mechanical properties is a source for optimism about the future of solid-state batteries, poor/heterogeneous wetting of the many explicit and implicit interfaces at and in the battery electrodes, and recent observations that Li dendrites may selectively proliferate into microdefect networks in some solid ceramic electrolytes to short-circuit battery cells [6,7] continue to pose fundamental barriers to progress.

An emerging practice is to fabricate the electrodes of solid-state battery cells with in-built ionic conducting pathways (*i.e.*, fabricate the cell using solid-state catholyte & anolyte, in addition to the solid-state electrolyte), to enable uniform ion transport. This strategy while satisfying a perhaps

obvious requirement for maintaining good access to the electrochemically active materials in a solid-state battery electrode introduce as obvious shortcomings, mostly because it lowers the volumetric and specific capacity of the electrodes and, by adding new fabrication steps, may also increase battery cost. Solid polymer electrolytes (SPEs) can be tailored to respond to imposed stress and thermal fields to overcome the wettability challenges faced by SSEs. They may also be formulated to achieve low volatility, high chemical & electrochemical stability in contact with Li metal, while at the same time maintaining good-enough mechanical properties to suppress non-planar/dendritic growth of the Li metal electrode.[5,8,9] Unfortunately, the most successful SPE (poly(ethylene oxide), PEO) is a semi-crystalline polymer, which crystallizes at temperatures in the range of 60 – 65°C. SPEs based on PEO polymer are therefore only able to achieve practically relevant ionic conductivity and meaningful ability to respond to stress or thermal fields to infiltrate the pores of the battery electrodes at temperatures somewhat above those targeted in the majority of applications.[10]

As a first step towards a solution, we recently reported a process whereby liquid electrolyte precursors based on 1,3-dioxolane (DOL) may be transformed to produce a solid-state ion-conducting material inside an electrochemical cell. The transformation is produced by initiating ring-opening polymerization of the liquid DOL using a Lewis acid salt ($AlCl_3$, $Al(OTf)_3$, *etc*.) dissolved in the electrolyte [11-14]. The approach has been shown to be effective in promoting reversible stripping and plating of Li by simultaneously limiting chemical and electrochemical side reactions with electrolyte components and promoting formation of stable solid electrolyte interfaces with Li. The solid-state electrolytes thus formed sustain stable cycling of Li||LFP full cells, provided suitable steps were taken to slow oxidative degradation of the poly(DOL) at the cathode and to limit corrosion of the cathode current collector by the Lewis acid initiator.[11] A

drawback nonetheless is that the ring-opening polymerization reaction is reversible, meaning that a broad distribution of macromolecular species is present in the battery cell at any given time,[11,14] which while beneficial for achieving high room-temperature ionic conductivity, makes it impossible to create sufficiently high molecular weight polymers to achieve electrolytes with the mechanical characteristics required for a solid-state battery.

Herein, we report on the synthesis, structure, thermal properties, and electrochemical characteristics of a family of hybrid SPEs formed inside an electrochemical cell. Created by $Al(OTf)_3$-initiated ring-opening polymerization of 1,3-dioxolane (DOL)/PEG-SiO_2 nanoparticle dispersions containing LiTFSI-$LiNO_3$ salt mixtures, the hybrid SPEs preserve the favorable features of the first-generation, in-situ formed poly(DOL) SPEs but also offer enhanced ion-transport, thermal and mechanical properties, which we attribute to the PEG-SiO_2 nanoparticle component. Significantly, the beneficial effects of the PEG-SiO_2 particles are already apparent at SiO_2 volume fractions as low as 3%, where the particles result in faster development of poly(DOL) mechanical modulus and a more than doubling of the room-temperature ionic conductivity of poly(DOL). Additionally, the PEG-SiO_2 nanoparticles produce dramatically lower activation energy barriers for ion transport — relative to electrolytes composed either of the pure poly(DOL) or pure PEG-SiO_2 materials. Small-angle X-ray scattering, thermal analysis, mechanical characterizations were used to understand the structural, thermal, and mechanical factors responsible for these improvements. By means of electrochemical analysis in Li||Cu half cells and Li||SPAN (Sulfur/polyacrylonitrile) full cells, we report further, that the hybrid SPEs facilitate stable electrochemical cycling of batteries that employ Li metal anode.

Polymer-ceramic hybrid materials provide a well-researched route for achieving free-standing SPEs with high mechanical strength and improved room temperature ionic conductivity (σ_{RT}).[5,15-

17] While the first of these features is intuitive, the second is not —it is believed to originate from suppression of crystallization of the polymer component, which promotes wetting and ion transport. The notoriously poor colloidal stability of small inorganic particles in polymers render most hybrid SPE designs impractical.[15,18-21] SiO_2 nanoparticles tethered with short (< 10 kDa molecular weight) PEG chains have been observed to form stable dispersions in polymers due to specific interactions between the dispersing medium and the tethered chains, enhanced particle curvature, and the fact that the space-filling constraint between tethers provides a strong thermodynamic incentive for polymer molecules not attached to the nanoparticles to fill the space between the cores.[22-25]

Nanoparticles composed of high dielectric constant SiO_2 nanocores ($\varepsilon = 3.6$; $d_{SiO2} \approx (10 \pm 2)$ nm) densely grafted with 5 kg/mol PEG chains were selected as candidates for the in-situ formed hybrid SPEs of interest in the present study. This choice was motivated by a number of considerations. The most important is that prior to ring-opening polymerization of DOL, it is essential to preserve simple, liquid-like flow properties in the DOL/PEG-SiO_2 hybrid liquid electrolytes to facilitate complete wetting of all interfaces inside a battery cell. A colloidally stable, unform dispersion of nanoparticles in a liquid host is a requirement for achieving this goal. Additionally, the PEG chains may serve at least three beneficial purposes. First, a densely grafted layer of PEG chains on each SiO_2 nanoparticle will enhance particle dispersion both by mechanisms outlined above and by the more obvious fact that the tethered chains will provide a steric barrier to prevent formation of particle aggregates. Second, by co-crystallizing with the host SPE molecules, the PEG chains will introduce disorder in crystalline domains of the host, reducing crystallite size and potentially lowering the SPE's melting temperature; we will show later that this is consistent with what is observed in our experiments. Third, the tethered PEG oligomers are themselves capable of

conducting Li ions. It means that the hybrid SPEs will present both bulk and interfacial pathways for ions to move in the electrolyte, which could provide synergistic enhancement in ionic conductivity. We note further that the SiO_2 cores impart other beneficial attributes. SiO_2 particles are known, for example, for their ability as additives in polymeric systems as they improve mechanical strength [26,27,29], electrical and dielectric properties [28,30,32], and flame resistance [31,32]. As a final consideration, we point to studies on PEG-SiO_2 hairy nanoparticles (HNPs) dispersed in poly(methyl methacrylate) (PMMA) which showed that the negative Flory-Huggins parameter, $\chi < 0$, between PEG and PMMA leads to very large enhancements in colloidal stability relative to what is achieved from the curvature and space filling effects discussed earlier.[33] Although the χ parameter for PEG/poly(DOL) mixtures has not been reported, results from thermal and small-angle scattering measurements in a chemically similar system, poly(ethylene glycol) dimethyl ether (mPEGm)/PEG-SiO_2 [34,35], reveal propensity for co-crystallization between the two chains.[36]

Ionic conductivity and activation energy of hybrid Poly(DOL)/SiO_2-PEG SPEs

Figure 1 reports the ionic conductivity of SPEs composed of poly(DOL), PEG-SiO_2, and poly(DOL)/ PEG-SiO_2 hybrids as a function of temperature. In every case the electrolytes were doped with 2 M LiTFSI salt and conductivity measured through dielectric relaxation spectroscopy (DRS) in coin 2032 cells. The main finding is that the room-temperature conductivity increases by 1.5 mS/cm (*i.e.*, is more than doubled) upon introduction of PEG-SiO_2 at a relatively moderate SiO_2 core particle loading, ϕ_c = 2.7 vol.%. High room-temperature (RT) ionic conductivity σ_{RT} values have previously been reported for poly(DOL) [11], our observation is that it is possible to further enhance these values by adding PEG-SiO_2 nanoparticles to the materials.

We wondered whether the improvements in room temperature ionic conductivity for the poly(DOL) SPEs are a consequence of changes (*e.g.*, slow-down) in the kinetics of ring-opening polymerization of DOL in the presence of the PEG-SiO_2 nanoparticles. We evaluated how the ionic conductivity for the hybrid SPEs evolve during the polymerization reaction for a fixed concentration (10 mM) of the $Al(OTf)_3$ initiator and fixed value of ϕ_c = 2.7 vol.%. In parallel we also studied how the dynamic elastic/storage, G', and loss, G'', moduli of the hybrid SPE's evolve with time. The results reported in **Figure 1b** show that within 1 hour of initiation, both moduli increase by nearly four orders of magnitude and reach stable steady-state values, indicating that at 10 mM $Al(OTf)_3$ the polymerization reaction progresses quite efficiently, at least in comparison to the pure poly(DOL) case reported later in **Figure 3a**. This behavior is like what is observed for σ_{RT}, which reaches a value of approximately 0.36 mS/cm after 1 hour and maintains conductivities close to that value (*e.g.*, 0.32 mS/cm) after ten days.

More remarkable, however, is how the temperature-dependent ionic conductivity $\sigma(T)$ evolves with time. Specifically, we observe a gradual transition from Volger-Fulcher-Tammann (VFT) to Arrhenius behavior as time increases. To understand this behavior, we note first that the VFT ($\log\sigma = \log\sigma_0 - \frac{B}{k_B(T-T_{VF})}$) and Arrhenius ($\log\sigma = \log\sigma_0 - \frac{E_a}{k_BT}$) models for ionic transport in SPEs differ primarily in the assumed mechanisms by which ions move in materials. The differences are reflected in the activation energy, E_a, and apparent activation energy, B, barriers for the transport. Here σ_0 is a preexponential factor, T is the absolute temperature, k_B the Boltzmann constant, $T_{VF} \cong T_g - 50$, is termed the Vogel-Fulcher temperature, T_g being the glass transition temperature of the SPE, which is determined to be 183 K for poly(DOL) with 10 mM $Al(OTf)_3$. It is apparent that the two models approximately converge when the thermodynamic temperature is recast as the temperature distance from the glass transition. Thus, while the VFT

model assumes that ions in a SPE move by a combination of normal diffusion through the medium and by coupled glassy motions of polymer chain segments, the Arrhenius model imagines that diffusion alone governs ion transport. This can be understood in physical terms by noting that when a material is cooled, density increases and the free volume decreases. Consequently, segmental motion is arrested, and ions can only move via diffusion.[37-39] The transition from VFT to Arrhenius within 24 hours of polymerization can then be understood to reflect gradual arrest of the segmental motions such that the coupled ion and chain dynamics characteristic of VFT changes to a dominantly ion-hopping/diffusion- based transport process.

Although both Arrhenius and VFT models can fit the $\sigma(T)$ curves well at all times, the VFT model fits the data best for the first 5 hours of polymerization, and the Arrhenius expression is best employed thereafter. In the first 5 hours, E_a is 0.71 ± 0.01 kJ/mol and is analyzed best using VFT fit. There is an increase in $B \approx E_a$ post 5 hour of polymerization along with a shift from VFT to Arrhenius-like behavior, with a constant B of 0.38 ± 0.021 kJ/mol observed over a period of 10 days, post the 5th hour. Curiously, decreasing the initiator content by ten-fold causes the conductivity value to increase by ten-fold, as seen in the case of 1 mM $Al(OTf)_3$ poly(DOL) with σ_{RT} = 3.75 mS/cm. As will be observed in the mechanical responses, lowering initiator content increases the molecular weight of the resulting poly(DOL), which in turn makes chains more flexible and less crystalline. Previous studies reported that the addition of 1 mM $Al(OTf)_3$ resulted in poly(DOL) with M_n of 8.5 kg/mol, M_w of 15 kg/mol (Polydispersity, $PDI = M_w/M_n \approx 1.8$), and DOL/poly(DOL) ratio of 14%.[11] The remaining unreacted DOL fraction in the system has been reported to further enhance the room-temperature ionic conductivity. Compared to poly(DOL) at the same 1mM initiator concentration and self-suspended PEG-SiO_2 (ϕ_c = 15 vol.%), the hybrid SPE with ϕ_c = 2.7 vol.% possesses the highest RT conductivity σ_{RT} = 3.75

mS/cm as well as the lowest activation energy E_a = 4.6 kJ/mol and maintain the highest σ_{RT} out of the three electrolyte systems within the experimental 50 K window. Addition of $LiNO_3$ expectedly increases σ_{RT} to 4.55 mS/cm and decreases E_a to 4.2 kJ/mol (Figure S3) due to higher mobile DOL fraction, as reflected in the lower moduli G'' and G' (**Figure 3d**). In contrast, self-suspended PEG-SiO_2 possess extremely low σ_{RT} of 0.2 nS/cm and significantly higher E_a of 32 kJ/mol. It has been reported that self-suspended PEG-SiO_2 behave as so-called soft glassy solids.[22,24,34,35,40] Two of the reported consequences include the change in PEG tethers to stretched conformation[24,34] as well as the caging phenomenon that is seen in strain-dependent mechanical property measurements (Figure S11).[22,24,35,40]

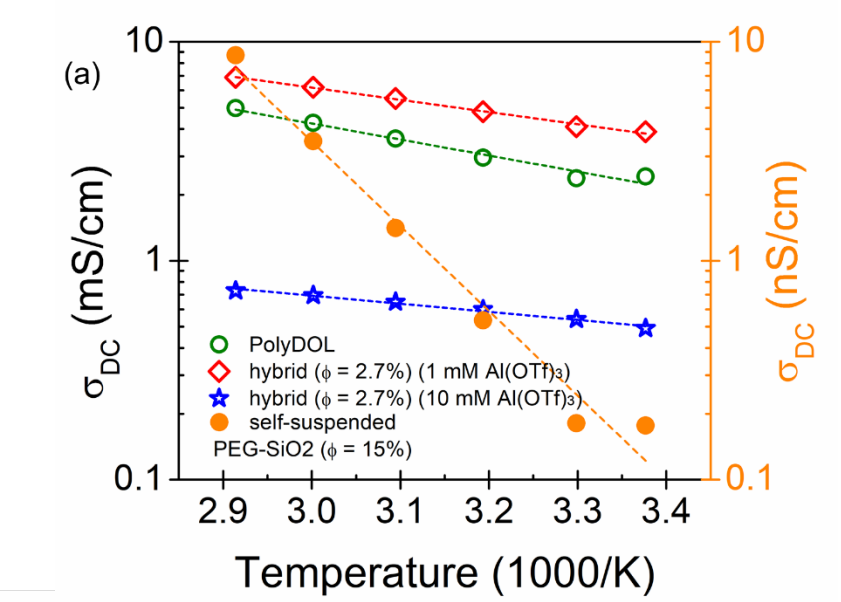
(a)
σ_{DC} (mS/cm)
σ_{DC} (nS/cm)
PolyDOL
hybrid (ϕ = 2.7%) (1 mM Al(OTf)3)
hybrid (ϕ = 2.7%) (10 mM Al(OTf)3)
self-suspended
PEG-SiO2 (ϕ = 15%)
Temperature (1000/K)

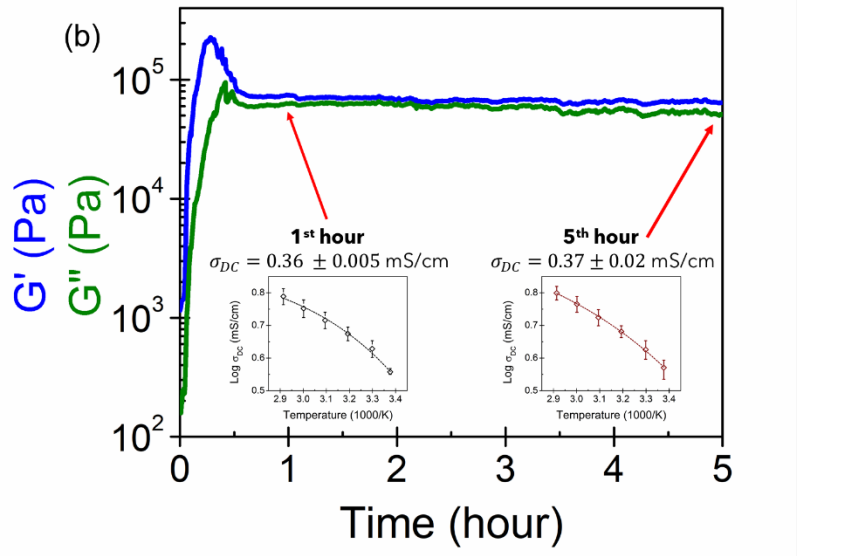
(b)
G' (Pa)
G'' (Pa)
1st hour
σ_{DC} = 0.36 ± 0.005 mS/cm
5th hour
σ_{DC} = 0.37 ± 0.02 mS/cm
Time (hour)

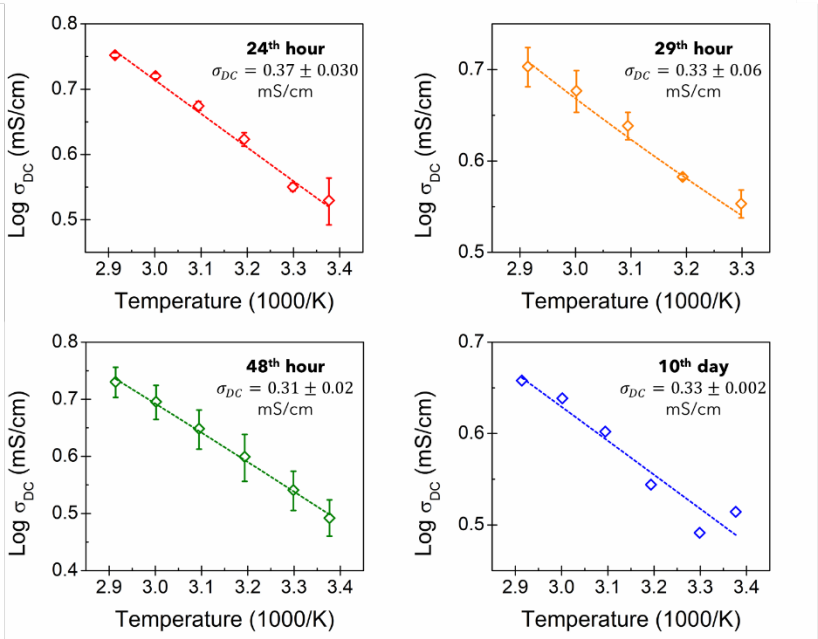
24th hour
σ_{DC} = 0.37 ± 0.030 mS/cm
29th hour
σ_{DC} = 0.33 ± 0.06 mS/cm
48th hour
σ_{DC} = 0.31 ± 0.02 mS/cm
10th day
σ_{DC} = 0.33 ± 0.002 mS/cm
Log σ_{DC} (mS/cm)
Temperature (1000/K)

Figure 1. Temperature-dependent conductivities of neat and hybrid samples probed through dielectric relaxation spectroscopy (DRS). **(a)** The conductivities of poly(DOL) (1 mM $Al(OTf)_3$, green open circles and 10 mM $Al(OTf)_3$, blue open stars), self-suspended PEG-SiO_2 HNPs (ϕ_c = 15 vol.%, orange closed circles), and hybrid system composed of both (ϕ_c = 2.7 vol.%, red open diamonds). All samples include 2 M LiTFSI salt. **(b)** Temperature-dependent DC conductivity of hybrid system (ϕ_c = 2.7 vol.%) polymerized with 10 mM $Al(OTf)_3$ for the 1st and 5th hour (as insets, shown with respect to time sweep result from Figure 2c), 24th hour, 29th hour, 48th hour, and 10th day of polymerization. Conductivity values shown in plots are room temperature conductivity and E_a values were fit either by Volger-Fulcher-Tammann (VFT) fit or Arrhenius depending on the best fit. Some error bars are smaller than the size of the scatter plot data points. Each DRS measurement was done over two samples and three iterations.

Structure and nanoparticle dispersion in hybrid SPEs

We used small-angle X-ray scattering (SAXS) to study the dispersion of PEG-SiO_2 nanoparticles in the hybrid poly(DOL)/PEG-SiO_2 SPEs. **Figure 2** reports our findings for HSPEs at different $Al(OTf)_3$ initiator concentrations. The results in **Figure 2a** shows that the scattered intensity $I(q)$ exhibits a plateau in the low q region and a scaling of q^{-4} in the high q region, for all initiator contents. Both characteristics are known features of scattering from dispersions well-distributed and unaggregated spheres.[34,41] Further insight on the dispersion state can be obtained by analyzing the structure factor $S(q)$. Based on previous experimental and theoretical studies[42-44], the peak in $S(q)$ at the lowest $q = q_1$ value reflects the repulsive interactions between hairy nanoparticles, while the peak at the next lowest $q = q_2$ reflects entropic attractions between PEG tethers. The interparticle distance is then defined as $d_{p-p} = 2\pi/q_1$ while distance between tethers can be estimated as $2\pi/q_2$.

Figure 2c indicates that both distances increase with increasing initiator content. This trend is typically observed with the dilution of homogeneous particle suspension, with larger interparticle

distances caused by less correlated cores.[35] The entropic attraction between tethers naturally decreases with dilution as it weakens the space-filling constraint of the tethers.[35] The increasing initiator concentration possesses similar effect as dilution, with both $2\pi/q_1$ and $2\pi/q_2$ increases with $Al(OTf)_3$ content. Radical polymerization including the ring-opening polymerization of DOL monomers is known to have the resulting polymer chain numbers depending significantly on initiator content. With higher initiator content, more radical sites are introduced during initiation process and during polymerization, higher termination rate at lower chain length is typically achieved.[45,46] This creates a greater number of shorter chains distributed throughout the system. These chains can behave similarly to solvent molecules surrounding the HNPs, thus increasing $Al(OTf)_3$ content has a similar effect to dilution. The polymerization process and kinetics of this hybrid system is further discussed through time sweep rheology measurement. The interparticle distance of self-suspended HNPs with ϕ_c = 11 vol.% is also presented in **Figure 2c**. It indicates that at the solvent-less, self-suspended form, the interparticle distance is d_{p-p} = 19 nm. This value is in a good agreement with estimated value from random close-packing model (d_{p-p} = 18 nm, Equations S3,S4).

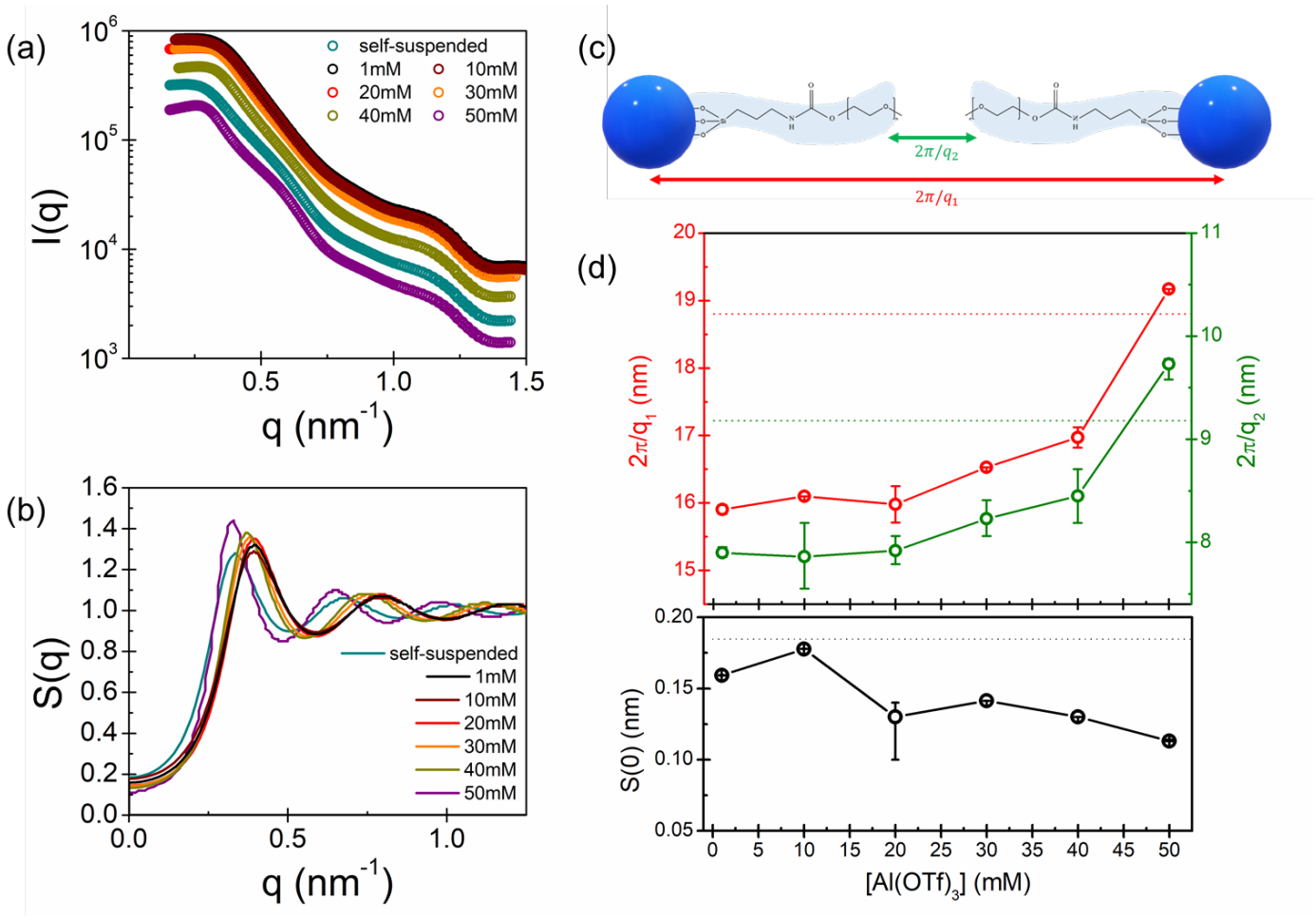

Figure 2. Small angle X-ray scattering (SAXS) profiles to determine structure of PEG-SiO_2 HNPs/poly(DOL) hybrid material. **(a)** Intensity profile and **(b)** structure factor of HNPs/poly(DOL) with ϕ_c = 2.7 vol.% with initiator $Al(OTf)_3$ content varying from 10 to 50 mM. **(d)** Structure factor analysis gives interparticle distance d_{p-p} (red data points) and distance between tethers (green data points) as described in the diagram **(c)**, as well as structure factor at q = 0. Dashed lines in (d) represent result for self-suspended HNPs with ϕ_c = 11 vol.%. Each measurement was done over two samples and three iterations.

The Structure factor in the limit of zero wave vector $S(0)$ is related to the isothermal compressibility of the material, which in the case of the hybrid SPEs reflects the ease with which long-range fluctuations in particle density can grow.[47,48] The results reported in **Figure 2d** indicate that density fluctuations initially decrease with increasing $Al(OTf)_3$ concentration, but

thereafter are largely insensitive to the initiator concentration. It was previously observed that the largest effect on $S(0)$ comes from two main sources: (i) poor dispersion of hairy nanoparticles in a host material [49]; and (ii) polydispersity in grafting density [42] of the hairy nanoparticles, *i.e.*, particles are composed of different number of tethers and this difference has a small but observable effect on the long-range density fluctuations. As the PEG-SiO_2 particle chemistry and concentration of DOL remains essentially unchanged with the changing initiator content, our results indicate that the SiO_2 nanocore dispersion in the poly(DOL) host remains largely unchanged. This result is consistent with the gross behaviors observed in $I(q)$ as well as $S(q)$ and confirm the anticipated benefits of constructing hybrid SPEs using polymerizable DOL and PEG-SiO_2 hairy nanoparticles as the structural building blocks.

Ring-opening polymerization kinetics

Considering the beneficial effects of the PEG-SiO_2 nanoparticles on room temperature ionic conductivity of the hybrid SPEs, an open question is whether nanoparticles achieve this effect by interfering in some way with the ring-opening polymerization of DOL. We investigated the polymerization reaction kinetics of 1,3-dioxolane (DOL) at room temperature by measuring the time-dependent evolution of the mechanical loss, G'', and storage, G', moduli (**Figure 3a**). Similar so-called "time sweep" mechanical measurements have been used to observe processes such as polymer degradation, crosslinking, and phase separation[50-52] that lead to time-dependent changes in polymer molecular weight and/or structure. A similar approach was also reported in our previous work for interrogating time-dependent growth of poly(DOL) when DOL is exposed to $Al(OTf)_3$.[11] As DOL monomers propagate to create longer poly(DOL) chains, both the elasticity, as measured by G', and the fluidity, as measured by G'', of the hybrid SPEs are expected to change as a function

284 of time. The results reported in **Figure 3** indicate that both G'' and G' rise rapidly at first and
285 plateau after approximately 20 minutes, with the G'' plateau typically larger than the plateau in G'.
286 This observation indicates that the fully polymerized SPEs are likely composed of low-molar-
287 mass, unentangled polymer chains. It is also considered favorable for an electrolyte because
288 viscous rather than elastic properties of the materials dominate, creating a structure with relatively
289 low resistance to ion motion and deformation.[53-55] The inset to **Figure 3a** reports the effect of
290 shear strain, γ, on G'' and G'after the plateau is observed, at the 30-minute time point during the
291 polymerization reaction. The results show that irrespective of the imposed strain, the hybrid SPE
292 response is dominated by viscous stresses that become less strain dependent as shear strain rises.
293 This leads to so-called shear-thinning behavior, which is a commonly seen characteristic of
294 amorphous, linear polymers.[53]
295 It is known, however, that ether-based polymers like poly(DOL) are semi-crystalline materials at
296 room temperature.[10] Crystallization creates discrete domains in the materials in which many
297 individual polymer chains are localized. This yields entanglement-like effects and elasticity in a
298 macroscopic material. Evidence of both behaviors are seen in long-time moduli measurements
299 reported in **Figures 3a** and **3b** where a cross-over from viscous to elastic dominant behavior is
300 observed, which is followed by another plateau regime where $G' > G''$. In this latter regime moduli
301 values reach 10^5 Pa and are comparable to those expected in melts of very high molecular weight
302 polyethers.[56] The second-stage moduli growth, and enhanced elasticity coincides with
303 observations of a recrystallization peak in differential scanning calorimetry (DSC) measurements
304 (Figure S4), consistent with its connection to crystallization of the poly(DOL).
305 As higher initiator content is often correlated to faster polymerization kinetics and shorter polymer
306 chains[46], the characteristic times for appearance of the first plateau would be expected to decrease

with increasing $Al(OTf)_3$ concentration, which is precisely what is observed (Figure S9). We define two characteristic times for the process. The first corresponds to the time (t_p) at which the first plateau is formed, and is considered a feature of the amorphous poly(DOL) polymer; the second time-scale (t_c) at which the second, elasticity-dominant, plateau is observed is attributable to formation of semicrystalline domains in the polymer. Indeed, while shorter polymer chains tend to crystallize more readily, they are known to possess lower mechanical strength (Figure S5).[55]

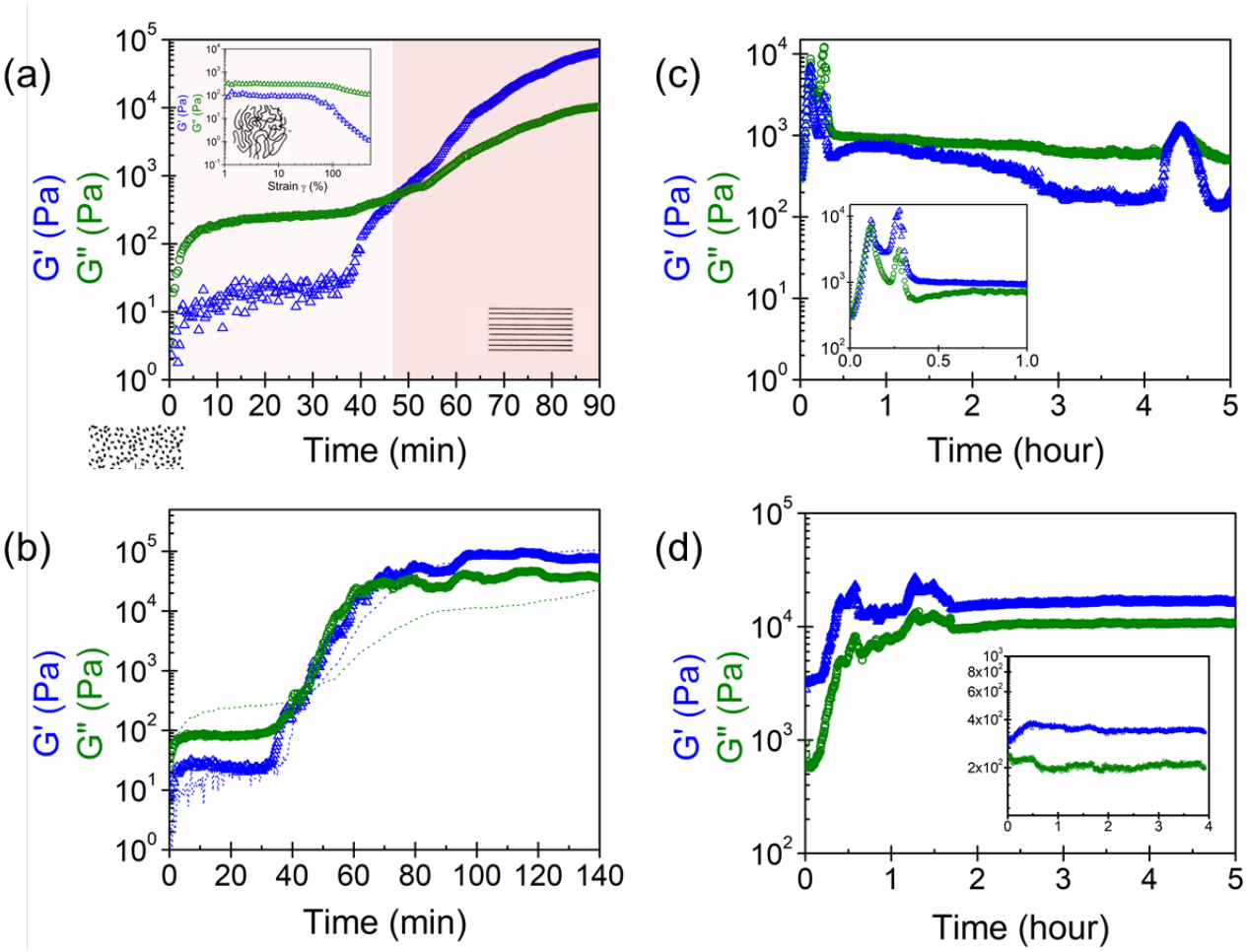

Figure 3. Time-dependent dynamic shear flow measurements are used to study changes in polymerization kinetics induced by PEG-SiO_2 HNPs in a poly(DOL) SPE. **(a)** Time sweep measurement of DOL monomers polymerized with 10 mM $Al(OTf)_3$ with the addition of: **(b)** 10 mM $LiNO_3$, **(c)** PEG-SiO_2 HNPs (ϕ_c = 2.7 vol.%). **(d)** DOL polymerized with 1 mM $Al(OTf)_3$ with PEG-SiO_2 HNPs (ϕ_c = 2.7 vol.%). This sample was measured using 25 mm cone and plate

geometry to ensure torque values above instrument's lower limit. The inset in (d) shows hybrid 1 mM initiator system with the addition of 2 M LiTFSI. The inset in (a) represents a strain sweep at 30-minute time-point during polymerization. The schematics of polymerization process going from monomers to amorphous polymer to polymer crystals were displayed in (a). Dashed line in (b) shows data point from (a) as a comparison between poly(DOL) polymerization with and without $LiNO_3$. The inset in (c) shows clearer peaks in G'' and G' at early time. All room temperature time sweep measurements were carried out at angular frequency of ω = 10 rad/s and strain of γ = 5%. Strain sweep was measured also at RT and ω = 10 rad/s. $Al(OTf)_3$ contents of 1, 20 – 50 mM for each type of sample are shown in Figures S5 and S6.

The results reported in **Figure 3c** indicate that hairy PEG-SiO_2 HNPs have profound effects on the evolution of both G'' and G' during polymerization of DOL. Specifically, as seen in the inset to **Figure 3c**, peaks in G'' and G' are observed at early times before either modulus reaches the first plateau. The number of peaks is reduced and the spacing between peaks lowered with increasing $Al(OTf)_3$ concentration (Figure S6), such that at 50 mM $Al(OTf)_3$ only a single modulus peak is observed. It is conjectured that the strong interaction between PEG tethers and poly(DOL) is responsible for both observations. In the first place (*i.e.*, before the formed poly(DOL) crystallizes), such interactions retard poly(DOL) chain growth by extending the observational window for the reversible polymerization – depolymerization reaction. This effect should disappear as the initiation rate for the ring-opening reaction becomes higher at higher $Al(OTf)_3$ concentration, which is consistent with what we observe.

The time at which the first G' peak (t_{pk}) is observed is reported in Figure S9. The results show that t_{pk} manifests an appreciable change with initiator content, which is again in line with our hypothesis that interactions of the PEG tethers and the poly(DOL) hinders polymer chain growth in the amorphous regime. Previous studies of radical polymerization in the presence of inorganic fillers, [57-59] show that there is normally a decrease of polymerization rate in the presence of filler

particles, attributed to interactions between fillers and monomers/polymers. Results reported in previous study[57] reveal, further, that fractions of macroradicals are immobilized in the interface region. The reduced compatibility between filler particles and growing macroradicals produces polymer chains with higher average molecular weight. This finding is consistent with our observation of increasing G'' and G' with increasing $Al(OTf)_3$ concentration as opposed to the opposite trend for poly(DOL) without PEG-SiO_2 nanoparticles. Other studies[58,59] made similar observations, noting that polymers adsorption on ceramic filler particles can drive spontaneous de-wetting of the particles by the suspending medium, producing phase separation near the filler surface.

Normally an increase in initiator concentration would lead to enhanced polymerization rate along with decreasing mechanical strength [45,46,60,61]. For the hybrid SPEs, however, we find more complex behaviors. In Figure S10, equilibrium moduli G''_{eq} and G'_{eq}, normalized to initial moduli G''_0 and G'_0, reveal that G''_{eq}/G''_0 and G'_{eq}/G'_0 both increase with $Al(OTf)_3$ concentration. There is also a more rapid increase in G' compared to G''; the difference becomes larger as the $Al(OTf)_3$ concentration increases. As the viscous portion of bulk material is reflected in the loss modulus, G'', we infer that there is a gradual arrest to the viscous dynamics in the system as initiator content is raised. This agrees with the observation of higher crystallinity in poly(DOL) synthesized at higher $Al(OTf)_3$ concentration, as well as with the lack the entanglements of the relatively shorter polymer chains.[54,55] Increasing $Al(OTf)_3$ concentration also causes a longer equilibrium time (t_{eq}) (Figure S9). For the SPE with 1 mM added $Al(OTf)_3$, however, the normalized moduli are higher in comparison to the 10 mM case. It is conjectured that as polymerization proceeds, M_w in the orders of 15 kg/mol is reached.[11] This value is larger than the predicted entanglement molecular

weight of poly(DOL) ($M_e \approx 1.2$ kg/mol [11]), resulting in an entangled poly(DOL) that expectedly has larger moduli than the shorter, unentangled poly(DOL) chains.

PEG chains tethered to particles facilitate mixing with host polymers such as PMMA, which exhibit strong enthalpic interactions with PEG.[62] These interactions have been reported to lead to slower dynamics of the host material, increasing the average relaxation time of PEG-SiO_2/PMMA[62] composites. They also alter the melting point and recrystallization temperature of PEG-SiO_2/mPEG due to co-crystallization of mPEG hosts and the tethered PEG chains.[35,36] Co-crystallization is observed in our PEG-SiO_2/poly(DOL) hybrids as a single recrystallization peak in DSC measurements reported in Figure S4. The results show further that both the crystallization and melting peaks are shifted to lower temperatures than seen in either pure poly(DOL) or the self-suspended PEG-SiO_2, indicating the inhibition of crystallization is mutual and strong. These findings confirm that the tethered chains interact strongly with the poly(DOL), providing a straightforward explanation for the uniform distribution of particles observed from the SAXS $I(q)$ profile (**Figure 2a**).

The role of Lithium nitrate ($LiNO_3$) as an electrolyte additive for stabilizing the interfaces formed between ether-based electrolytes, including DOL and dimethylether (DME), and metallic Li anodes is well-known [63,64,76] and extensively studied, particularly in the context of Lithium-Sulfur (Li-S) batteries.[63,64,69] $LiNO_3$ is also thought to be advantageous in Li-S batteries because it inhibits lithium polysulfide (LiPS) shuttling,[67,68] which improves the cell-level cycling efficiency in ether-based electrolytes.[69,70] Although the source of these improvements is conventionally thought to be the unique chemistry and physical properties of the interfacial materials phases (interphases) ether-$LiNO_3$-LiPS mixtures form upon chemical and electrochemical reduction at a Li electrode, our recent study indicates that $LiNO_3$ may also produce strong coupling between

ether oxygens to produce polymer-like bulk material behavior in liquid ethers.[11,65] Paired with LiFSI, infrared spectroscopy in fact shows that cyclic DOL molecules are highly strained in the presence of $LiNO_3$ and appear less prone to undergo ring-opening polymerization. **Figure 3b** compares the time-dependent growth of G'' and G' in $Al(OTf)_3$-initiated polymerization of DOL in systems with (data points) and without (dashed line) $LiNO_3$. We find that the greatest effects of $LiNO_3$ is in increasing the induction time before the moduli begin to grow. Once the growth starts, $LiNO_3$ does not appear to have any significant effect on the polymerization reaction kinetics. The plateau G'' and G'values are also largely insensitive to $LiNO_3$, implying that the poly(DOL) structure in both the amorphous and crystalline state are unaffected by $LiNO_3$. Our results therefore imply that $LiNO_3$ is perhaps better thought of as a retardant than an inhibitor for the ring-opening polymerization of DOL. Importantly, we show in Figures S7 and S8 that these findings hold true for all measured $Al(OTf)_3$ concentrations. Retarders typically produce slightly larger rate of secondary radical generation, compared to primary radical generation ($k_{R2}/k_{R1} < 10$), resulting in secondary radicals with chemical and electronic structure, polarity, and stereochemical properties different than those of the propagating radicals.[66] This also means that they have different reactivity, which may alter macrokinetics depending on the rate of reaction between the secondary radicals and monomer molecules, features that will require further study.

Figure 3d reports the time-dependent moduli during polymerization of DOL in electrolytes containing both $LiNO_3$ and PEG-SiO_2 hairy nanoparticles. At low $Al(OTf)_3$ concentration (*i.e.*, 1 mM), the depolymerization reaction dominates over ring-opening polymerization, and the moduli are low. As the $Al(OTf)_3$ concentration is increased, the forward polymerization begins to dominate and an equilibrium elastic modulus, G' of 10^3 Pa is achieved at 50 mM $Al(OTf)_3$. We employ hybrid poly(DOL) synthesized with 1 mM $Al(OTf)_3$ initiator for all electrochemical

studies to follow. This initiator concentration is twice that used by Zhao, et al.[11] and is deliberately chosen to achieve larger degrees of ring-opening polymerization. We will show later that $LiNO_3$ plays a crucial role as a salt additive in such electrolytes, allowing Li to achieve highly reversible cycling when poly(DOL)/PEG-SiO_2 hybrid SPEs are employed as electrolytes in battery cells.

Electrochemical cycling of Li anodes in poly(DOL)/PEG-SiO_2 hybrid SPEs

Results in **Figure 4a** indicate that the coulombic efficiency (CE) of hairy nanoparticles-containing hybrid electrolyte (orange circles) in Li||Cu electrochemical cell is improved markedly to values as high as 99% upon addition of $LiNO_3$ to these electrolytes. A similar effect is seen for liquid DOL electrolyte (black circles), where addition of $LiNO_3$ also produces an increase of the CE to values as high as 97%. In the case of DOL, it was reported [65] that CE values as high as 99% could be achieved in dual-salt electrolytes containing both LiTFSI and $LiNO_3$. This effect was also observed for other electrolytes such as ethylene carbonate (EC), dimethyl carbonate (DMC), and dimethoxyethane (DME).[65] Polymerization from DOL to poly(DOL) reportedly also increases the CE.[11] The addition of $LiNO_3$ has been reported to lower DOL reactivity over a wide potential range, which is likely also partially responsible for the large improvements in CE observed. Chronoamperometry measurements using HSPEs with ϕ_c = 2.7%, with and without the addition of 0.5 M $LiNO_3$ (Figure S12), support these conclusions. In these experiments we held the voltage fixed at progressively lower values, approaching the Li electrode reduction potential. The measured leakage current at the intermediate voltages reflect reduction of electroactive species in the electrolyte, including the PEG chains tethered to the HNPs our case.[75] The results show that the leakage currents from the in-situ formed poly(DOL) hybrid electrolytes containing $LiNO_3$ are generally lower.

Previous works highlight the role of $LiNO_3$ additive in creating a stable layer that limit contact between electrolyte and Li-metal.[44,67,69,76] This passivation layer allows for a more homogenenous SEI.[77-78] To evaluate the first effect, electrochemical impedance spectroscopy (EIS) was performed for both systems in Li||Cu electrochemical cell upon holding potential for 1000 s at 0.2 V (Figure S12). It is seen that interfacial impedance of HNPs/PolyDOL with $LiNO_3$ is lower compared to the hybrid system without $LiNO_3$, indicated by the smaller semicircle in the imaginary impedance $Im(Z)$ – real impedance $Re(Z)$ plot. This Nyquist plot shows a single semicircle for both systems, and the bulk resistance can be fitted in series with a charge-transfer resistance that is in parallel with a double-layer capacitance.[79] This results in interfacial resistance of 107 Ω for hybrid without $LiNO_3$ and a lower value of 76.5 Ω for hybrid electrolytes the contain $LiNO_3$. When the impedance is evaluated after different potential steps in chronoamperometry (Figure S12), hybrid electrolyte containing $LiNO_3$ is seen to possess high interfacial stability with a uniform value of impedance while the electrolyte without shows increasing value of interfacial impedance with more reduction at lower potential. There is an increase in the interfacial impedance of HSPEs compared to poly(DOL) SPEs in Li||Li electrochemical cell due to the addition of PEG-SiO_2 HNPs (Figure S13). It is expected that HNPs add to the thickness and composition of the SEI, thus adding to the interfacial resistance. Results from scanning electron microscopy (SEM) paired with energy-dispersive X-ray spectrosopy (EDS) on lithium plated on copper foil at 10 mAh/cm^2 indicates the presence of well-distributed elemental silicon without any large aggregates observed (Figure S14). As an initial proof of concept and to illustrate the potential practical benefits of our HSPEs we fabricated Li-S batteries composed of Sulfur/polyacrylonitrile (sPAN) cathode (**Figure 4c**), metallic Li foil as anode, and the HSPE (ϕ_c = 2.7%) with and without 0.5 M $LiNO_3$ as electrolyte. The results show that, but for the first cycle, the CE for the HSPEs is high and stable. After an

initial period of decay, the discharge capacity (**Figure 4c**) also shows good stability at constant current density, as well as good responsiveness to changes in current density (**Figure 4d**) in the range 0.1 mA/cm^2 (=0.1C) to 1 mA/cm^2 (=1.0C). Notably, when the C-rate is reduced to its original value of 0.1C following higher rate cycling, a good capacity retention of ~90% is seen compared to the steady value of the first few cycles. Previous Li||sPAN results for DOL/DME electrolyte resulted in more than 60% capacity loss within the first 50 cycles[81]. A decay in capacity was also observed in Li||sPAN for HSPEs due to DOL electrolyte reaction with sPAN, which produces lithium polysulfides that are observable under UV-Vis spectroscopy[81]. The amount of polysulfide products could be reduced by coating sPAN cathode with thin Nafion coating (Figure S15). As a second example, we also investigated the electrolytes in Li||LFP cells (Figure S16). It is shown that despite larger capacity fade in HSPEs before stabilizing, hybrid electrolyte possesses higher discharge capacity throughout the cycle range presented as well as a more stable overpotential value. Stable plating and stripping for symmetric Li||Li cell for > 250 hours and electrochemical stability up to 4.75 V in Li||SS cell were also observed (Figure S17).

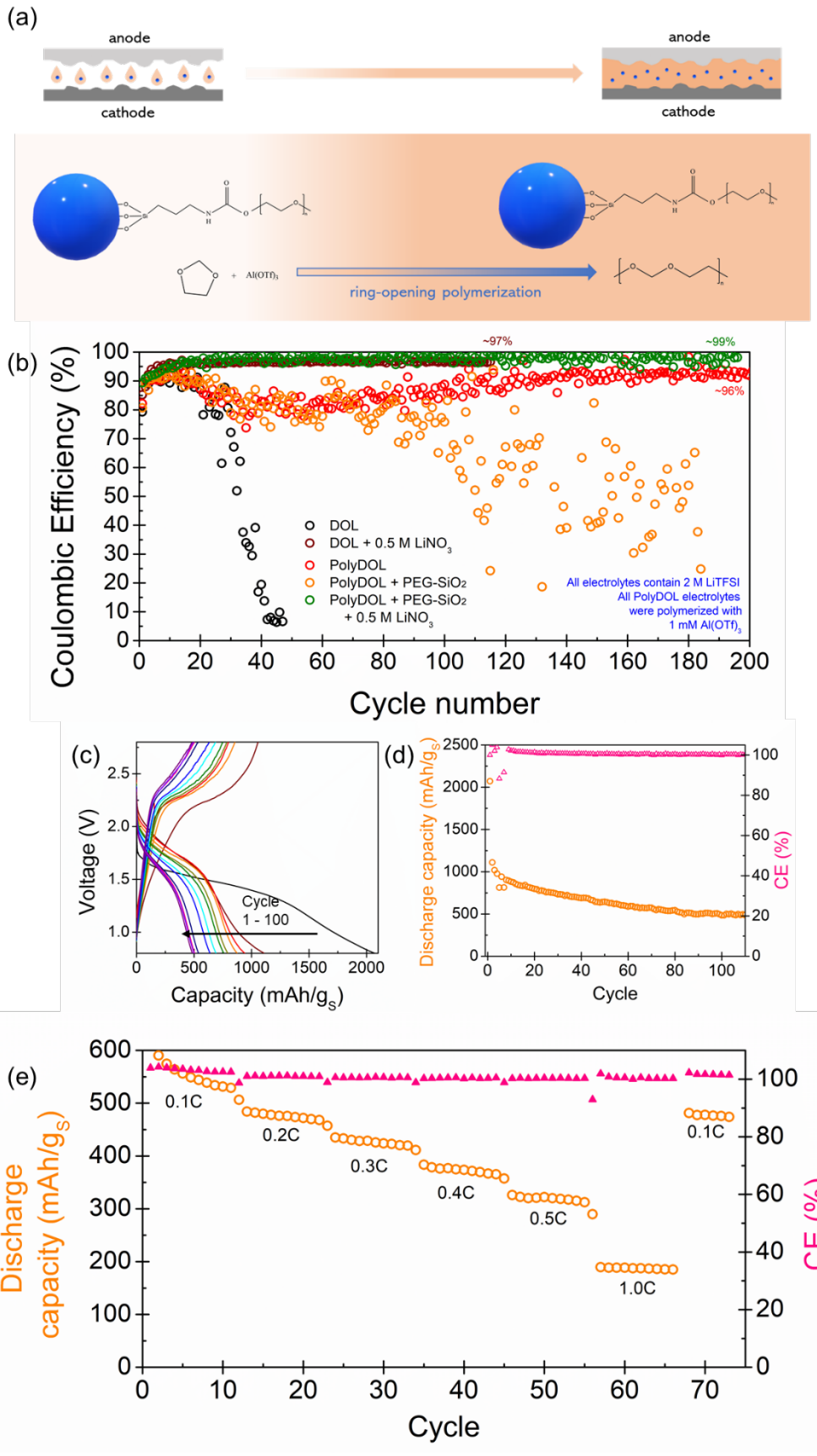
(a)
anode
cathode
anode
cathode
ring-opening polymerization
(b)
Coulombic Efficiency (%)
Cycle number
~97%
~99%
~96%
DOL
DOL + 0.5 M LiNO3
PolyDOL
PolyDOL + PEG-SiO2
PolyDOL + PEG-SiO2 + 0.5 M LiNO3
All electrolytes contain 2 M LiTFSI
All PolyDOL electrolytes were polymerized with 1 mM Al(OTf)3
(c)
Voltage (V)
Capacity (mAh/gS)
Cycle 1 - 100
(d)
Discharge capacity (mAh/gS)
CE (%)
Cycle
(e)
Discharge capacity (mAh/gS)
CE (%)
Cycle
0.1C
0.2C
0.3C
0.4C
0.5C
1.0C
0.1C

473

Figure 4. Electrochemical performance of HNPs/poly(DOL) hybrid electrolyte. **(a)** Schematic of in-situ polymerization of DOL in the presence of HNPs. Slurry of HNPs, monomer, and initiator was added, ensuring good wettability before the mixture was let sit for at least 24 hours of polymerization process. **(b)** Coulombic efficiency (CE) of various poly(DOL) electrolyte and hybrids containing PEG-SiO_2 HNPs (ϕ_c = 2.7%) with and without 0.5 M $LiNO_3$ at 0.1 mA/cm^2 in Li||Cu cells **(c)** Galvanostatic cycling profile for Li||sPAN cell with hybrid electrolyte containing ϕ_c = 2.7%, 2 M LiTFSI, and 0.5 M $LiNO_3$, with discharge capacity and Coulombic efficiency (CE) over cycle shown in **(d)**. Rate performances for the Li||sPAN cells at different c-rates are shown in **(e)** with 1.0C is current density of 1 mA/cm^2. All electrolytes include 2 M LiTFSI salt and all PolyDOL electrolytes were polymerized with 1 mM $Al(OTf)_3$. Galvanostatic cycling profile for Li||LFP cell with the same electrolyte along with its discharge capacity profile and Coulombic efficiency (CE) is presented in the Figure S16.

Conclusions

It is reported that ring-opening polymerization of DOL containing PEG-SiO_2 hairy nanoparticles can be used to synthesize hybrid solid-state poly(DOL) electrolytes inside a battery cell at various initiator contents. The PEG-SiO_2 structures hinder crystallization of poly(DOL), which leads to a substantial increase in room-temperature ionic conductivity σ_{DC} of the hybrid electrolytes, relative to the neat (particle-free) poly(DOL) SPE. The effect is synergistic in that the hybrid electrolyte also manifests a dramatically higher σ_{DC} — from nS/cm-scale to mS/cm scale values, in comparison to SPEs composed entirely of the PEG-SiO_2. The structure of dispersion was studied through small-angle X-ray scattering (SAXS), and it is observed that the PEG-SiO_2 particles are well dispersed in their poly(DOL) host. Analysis of the structure factor $S(q)$ deduced from SAXS indicates that both the distances between nanoparticles and PEG tethers increase with increasing initiator content. Increasing initiator content is thus seen to have an effect analogous to dilution of nanoparticles in a suspending host. SAXS also reveals a decrease in long-range density fluctuations, as reflected in the decreasing value of $S(0)$ with increasing initiator content. Time-

dependent mechanical shear analysis indicate that the SiO_2-PEG particles alter polymerization kinetics and that this effect is enhanced by addition of $LiNO_3$ salt additive. These measurements also reveal a competition between polymerization-depolymerization processes, which manifests as peaks in moduli G'' and G' at early times. Eventually, at high initiator content, the maxima coalesce, consistent with a polymerization process in which the forward ring-opening reaction dominates the reverse reaction, resulting in higher molecular weight poly(DOL). Inclusion of $LiNO_3$ retards ring-opening polymerization and manifests as a longer induction time, but otherwise has no effect on the polymerization process.

The enhancement in room-temperature ionic conductivity relative to SPEs composed of self-suspended PEG-SiO_2 is attributed to the shift from arrested soft-glassy dynamics to polymer-like behavior. Hybrid SPEs with ϕ_c = 2.7 vol.% are found to exhibit lower energy E_a = 4.6 kJ/mol, compared to poly(DOL) at the same initiator content and self-suspended PEG-SiO_2 HNPs. Addition of $LiNO_3$ increases σ_{RT} to 4.55 mS/cm and decreases E_a to 4.2 kJ/mol. The higher fraction of mobile ion carriers is thought to be the reason to this high σ_{DC} and low E_a. Evaluation of the in situ-formed PEG-SiO_2 HNPs-poly(DOL) electrolytes in Li||Cu half cells, revealed high Coulombic efficiency (CE) and excellent Li reversibility, particularly in electrolytes where $LiNO_3$ is used as an additive. The resulting hybrid PolyDOL electrolyte was finally evaluated in Li||SPAN full cells and demonstrated to support enhanced battery cycling.

Materials and Methods

Material Preparation

Synthesis of PEG-tethered SiO_2 nanoparticles

Silica nanoparticles (LUDOX SM30, 10 ± 2 nm), poly(ethylene glycol) monomethyl ether (mPEG-OH) with M_n = 5 kDa, 3-(triethoxysilyl)propyl isocyanate, 1,4-diazabicyclo [2.2.2.]-octane (DABCO), and anhydrous dichloromethane were purchased from Sigma-Aldrich. PEG-tethered silica nanoparticles were synthesized according to a previously reported method.[34,35] mPEG-OH (10.0 g, 2.00 mmol), 3-(triethoxysilyl)propyl isocyanate (0.495 g, 2.00 mmol), and DABCO (0.336 g, 3.00 mmol) were dissolved in anhydrous dichloromethane (10.0 mL) and reacted at 50°C for 48 hours. The resulting mixture was precipitated into excess hexanes. mPEG-silane was isolated by decantation before drying in vacuo at room temperature. The resultant dry, pure mPEG-silane was stored at 2 – 8°C prior to usage.

The silica nanoparticles (1.82 mL) were diluted in excess deionized water (400 mL) and a solution of mPEG-silane (2.00 g) in deionized water (50.0 mL) was added dropwise. The mixture was reacted at 70°C for 48 hours. The reacted mixture was dried partially in a convection oven at 45°C for 24 hours before further purification by repeated centrifugation in a 1:4 (v/v) chloroform/hexanes at 8500 rpm. Self-suspended hairy nanoparticles were dried further in vacuo at room temperature before storage under argon atmosphere. Differential scanning calorimetry (DSC) shows that self-suspended HNPs forced PEG chains to only adopt extended conformation due to space-filling constraint [24] (Figure S1). The grafting density and core volume fraction can be varied by adjusting the ratio of SiO_2 nanoparticles to the mPEG-silane. Thermogravimetric analysis (TGA) was employed to determine the weight fraction of the undegraded inorganic content, which can be translated to the core volume fraction of SiO_2 and grafting density (Figure S2 and Equations S1,S2).

Dispersion of HNPs in poly(DOL)

1,3-dioxolane (DOL) and Aluminum trifluoromethanesulfonate ($Al(OTf)_3$, 99.9% metals basis) were purchased from Sigma-Aldrich, and Lithium nitrate ($LiNO_3$, 99.9% metals basis) was purchased from Chem-Impex Int'l, Inc. Due to aggregation of self-suspended HNPs and hydrophilicity of DOL, room-temperature ultrasonification of HNPs in DOL was not an accessible method. HNPs were dispersed in deionized water (15.0 mL) and dispersion was freeze-dried for 72 hours to ensure minimal water content. The resulting HNPs were no longer aggregated and can be easily dispersed in PolyDOL precursors through mechanical shaking. The unaggregated, flake-like HNPs were dried in vacuo at room temperature for at least 24 hours before stored under argon atmosphere. HNPs (0.10 g) and $Al(OTf)_3$ initiator were added to DOL (1.00 mL) and DOL was let polymerized in presence of HNPs. Various initiator content was employed for X-Ray scattering and rheology measurements, ranging from 1 mM (1.89 mg in 4.00 mL DOL) to 50 mM (23.7 mg in 1 mL DOL). For time-dependent measurement involving $LiNO_3$, $LiNO_3$ (0.69 mg, 10 mM) was similarly added to DOL (1.00 mL) precursors. Core volume fraction for 0.10 g HNPs in 1.00 mL poly(DOL) was evaluated through TGA in Figure S2.

Electrolyte preparation

All electrolytes were prepared in argon glove box (Inert Inc.) with O_2 and H_2O content lower than 0.5 ppm. Lithium bis(trifluoromethanesulfonyl)imide (LiTFSI, puris., ≥ 99.0%) was purchased from Sigma-Aldrich. All electrolytes containing HNPs were further dried chemically with Li-strips, reacted in electrolyte solution at 60°C for 1 hour. All electrochemical tests utilized coin 2032 cells with Lithium foil as the anode and Celgard 3501 as the separator. Half cells were assembled with copper foil as the cathode and full cells were assembled with sulfur/polyacrylonitrile (sPAN) and lithium iron phosphate (LFP). LFP cathodes were prepared by a procedure previously outlined[11] with LFP loading of 4 mg/cm^2 and the preparation of sPAN

cathodes was previously done[81] with Sulfur loading of 0.5 mg/cm^2. sPAN cathodes were coated by dropping ~20μL diluted 1:10 Nafion:ethanol solution onto 3/5" sPAN and vacuum drying at 60°C.

Characterization Methods

Small-angle X-Ray scattering (SAXS)

SAXS measurements were conducted using Anton Paar SAXSess bench-top X-ray scattering system. The system employed a line collimated beam at 0.1542 nm and a block camera setup for data collection. All samples were measured at 70°C, which is above the melting point of samples. The experimental line collimated intensity $I_{exp}(q)$ is a function of point collimated intensity $I_0(q)$ [41,47] such that,

$$I_{exp}(q) = \int_{-\infty}^{\infty}\int_{-\infty}^{\infty} W_x(x)W_y(y)I_0\left(\sqrt{\left(\frac{\lambda a q}{2\pi} - y\right)^2 + x^2}\right) \quad (1)$$

$W_x(x)$ and $W_y(y)$ are the horizontal and vertical X-ray beam, x and y are the horizontal and vertical dimensions, q is the scattering wave vector, and a is the sample-to-detector distance. Generalized indirect Fourier transformation (GIFT) was utilized to desmear $I_{exp}(q)$ in obtaining $I_0(q)$. Particle scattering intensity $I_{particle}$ is defined in terms of the scattering intensity of particles in suspending medium $I_{particle/medium}$, scattering intensity of suspending medium I_{medium}, and volume fraction of suspending medium ϕ_{medium}.[82]

$$I_{particle} = I_{particle/medium} - \phi_{medium}I_{medium} \quad (2)$$

For spherical particles [41,40], scattering intensity of particles is

$$I_{particle}(q) = \phi_c \Delta\rho_e^2 V P(q) S(q) \quad (3)$$

where ϕ_c is the core volume fraction, V is the volume of a single particle, $\Delta\rho_e$ is the electron density contrast, $P(q)$ is the form factor, and $S(q)$ is the structure factor. The interparticle

correlations vanish at the dilute limit, causing the structure factor to be $S(q) \rightarrow 1$ and the form factor $P(q)$ can be obtained directly from the scattering intensity. Bare charge-stabilized SiO_2 nanoparticles (LUDOX SM30) was measured in a diluted aqueous suspension to obtain the $P(q)$. $S(q)$ was then obtained through GIFT method involving the Percus-Yevick closure relation that utilized a hard sphere structure factor model.

Thermogravimetric analysis (TGA)

The inorganic SiO_2 content of self-suspended PEG-SiO_2 hairy nanoparticles and their suspensions was estimated using thermogravimetric analysis (TGA) (TA Instruments Q500). TGA was performed under a nitrogen atmosphere from 20°C to 600°C at 10°C/min ramping rate. The self-suspended HNPs used for SAXS measurement were found to have 17 wt.% inorganic weight fraction, translating to 11 vol.% core volume fraction. The hybrid used in SAXS were found to have 4.2 wt.% inorganic weight fraction, translating to 2.7 vol.% core volume fraction. A sample calculation for the former is provided under Equations S1,S2 along with the estimation of tether density.

Mechanical rheology measurements

Oscillatory shear measurements were performed using a strain-controlled ARES-LS rheometer (Rheometric Scientific) with a cone and plate geometry (10 mm, 4° cone angle) or otherwise stated. Time-dependent measurements were carried out at room temperature with angular frequency of ω = 10 rad/s and strain of γ = 5%. Strain-dependent measurements were measured at 70°C with ω = 10 rad/s. Self-suspended HNPs were also measured at 70°C, above their melting point, with ω = 0.25 rad/s. Reaction components were mixed inside glove box and loaded on the rheometer only after induction time ends, which is signaled by an apparent change in viscosity.

Dielectric relaxation spectroscopy (DRS)

DC conductivity measurement was carried out using a Novocontrol broadband dielectric/impedance spectrometer. The same coin 2032 cells without electrodes were utilized, with Teflon ring containing the dried electrolytes. Conductivity was measured at room temperature before temperature was increased from 30°C to 70°C, and measurement with frequency of 10^7 – 1 Hz was done every 10°C. The conductivity value was taken to be the value at the frequency at which the maximum of $\tan(\delta)$ was seen. Arrhenius or Volger-Fulcher-Tammann (VFT) equations were used to fit the conductivity of the electrolytes, depending on the case as shown in results and discussions.

Differential scanning calorimetry (DSC)

DSC (TA Instruments Q2000) was adopted to evaluate thermal transitions of the self-suspended HNPs and hybrid samples. Thermal transitions were measured under nitrogen flow at a fixed ramp rate of 5°C/min. Hybrid materials were first heated to 70°C to remove thermal history before brought down to -100°C and heated back up to 70°C. Thermal history erasure of self-suspended HNPs was done by first heating to 100°C, followed by data collection in the second cycle with cooling to -150°C and subsequent reheating to 100°C. Measurements during the second heating cycle were used to evaluate the melting temperature T_m, recrystallization temperature T_c, and heat of melting ΔH_m that translates to crystallinity.

Electrochemical Measurements

Galvanostatic lithium stripping/plating tests were operated using Neware CT-3008 battery tester at room temperature, with current density of 1 mAh/cm^2 for asymmetric Li||Cu cells. Galvanostatic discharge/charge tests for Li||sPAN cells were done under also done under room temperature with current density of 0.1 mAh/cm^2. Li||LFP cells were charged and discharged at 0.1 mAh/cm^2 for the first cycle and 0.2 mAh/cm^2 for the following cycles. Chronoamperometry profiles and linear

sweep voltammetry were obtained using CH 600E electrochemical workstation at room temperature. Potentials were held at 2.0, 1.8, 1.6, …, 0.2 V for 500 seconds in chronoamperometry measurement. Plateaus were observed by the end of the 500-s mark. Potentials were varied from 2.5 V to 5.5 V with 1 mV/s scan rate on Li||SS (stainless steel) cell in linear sweep voltammetry measurement. Electrochemical impedance spectrometry (EIS) measurements were performed using a Solartron Frequency Response Analyzer (Model 1252) with frequencies ranging from 50 kHz to 10 mHz and at an amplitude of 10 mV.

Scanning Electron Microscopy (SEM)

Scanning electron microscopy (SEM) was done on Zeiss Gemini 500 scanning electron microscope with energy-dispersive X-ray spectroscopy (EDS) installed. The surface of characterized Lithium was plated on copper foil for 10 mAh/cm^2.

UV-Vis Spectroscopy

UV-Vis spectra were obtained through the use of Molecular Devices SpectraMax M2. sPAN and Nafion-coated sPAN were immersed in DOL electrolyte containing 2 M LiTFSI and 0.5 M $LiNO_3$ for 10 days before spectroscopy measurement.

Statistical Analysis

All data processing and statistical analyses were performed using the Origin software. With the exception of the Small-angle X-ray scattering (SAXS) data reported in Figure 2, there was no pre-processing of data prior to the analysis in Origin. All data was transported as comma-separated values (CSV) from software connected to each instrument. Arrhenius and Volger-Fulcher-Tammann (VFT) equations were used to fit the conductivity data, as detailed in the discussions related to results reported in Figure 1. The SAXS data in Figure 2 was fitted to determine the form factor and to remove background scattering; the procedure is discussed in the SAXS experimental

method section. No statistical analysis was done on the rheology data (Figure 3) or electrochemical performance data (shown in Figure 4). Replicate analysis of results from SAXS and DRS measurements were performed for two samples with three measurements each. The resulting mean ± SD values are indicated as confidence intervals/error bars in Figures 1b and 2d.

Associated Content

The effect of tethering PEG to SiO_2 on the melting point of self-suspended HNPs is compared with the analagous effects for the HSPEs. The procedures for determining the SiO_2 core volume fraction and for estimating the PEG grafting density on the SiO_2 particles is presented. Temperature-dependent ionic conductivity of hybrid SPEs containing $LiNO_3$ is reported. Time-dependent rheology measurements at different $Al(OTf)_3$ concentrations complementary to those presented in Figure 2. Characteristic times in DOL polymerization kinetics and the effects of initiator concentration on PolyDOL polymerization. Electrochemical impedance spectroscopy (EIS) and chronoamperometry results with HNPs and $LiNO_3$ addition. Surface images of Lithium plated at 10 mAh/cm^2. Galvanostatic cycling profile of hybrid electrolyte in Li||LFP cell. UV-Vis spectroscopy of electrolyte post sPAN immersion. Electrochemical stability window and symmetric Li||Li plating and stripping.

Author Information

Nyalaliska W. Utomo ORCID: 0000-0001-8855-6297

Yue Deng ORCID: 0000-0002-1683-5884

Qing Zhao ORCID: 0000-0003-0625-9892

Lynden A. Archer ORCID: 0000-0001-9032-2772

Acknowledgements

This work was supported by the Department of Energy Basic Energy Sciences Program through Award DE-SC0016082 and the National Science Foundation Partnerships for Innovation Program through Award no. # IIP-1919013. This work made use of the Cornell Center for Materials Research Shared Facilities which are supported through the NSF MRSEC program (DMR-1719875).

Conflict of Interest

LAA holds a financial interest in Sionic Technologies, a battery company commercializing Li-ion and Li-sulfur electrolytes based on multifunctional additives dispersed in liquid electrolytes.

Data Availability

The data that support the findings of this study are available from the corresponding author upon reasonable request.

Keywords

Solid-state Lithium metal battery, solid polymer electrolyte, in-situ polymerization, hairy nanoparticles, nanoparticle dispersion in polymeric host.

References Cited

[1] Takada, K., Acta Mat., **2013**, *61*, 759-770.

[2] Hatzell, K. B., Chen, X. C., Cobb, C. L., Dasgupta, N. P., Dixit, M. B., Marbella, L. E., McDowell, M. T., Mukherjee, P. P., Verma, A., Viswanathan, V., Westover, A. S., Zeier, W. G., ACS Energy Letters, **2020**, *5*, 922–934.

[3] Manthiram, A., Yu, X., Wang, S., Nat. Rev. Mater., **2017**, *2*, 16103.

[4] Famprikis, T., Canepa, P., Dawson, J.A., Islam, M.S., Masquelier, C., Nat. Mater., **2019**, *18*, 1278-1291.

[5] Li, S., Zhang, S.-Q., Shen, L., Liu, Q., Ma, J.-B., Lv, Wei, He, Y.-B., Yang, Q.-H., Adv. Sci., **2020**, *7*, 1903088.

[6] Garcia-Mendez, R., Smith, J.G., Neuefeind, J.C., Siegel, D.J., Sakamoto, J., Adv. Energy Mater., **2020**, *10*, 2000335.

[7] Kazyak, E., Garcia-Mendez, R., LePage, W.S., Sharafi, A., Davis, A.L., Sanchez, A.J., Chen, K.-H., Haslam, C., Sakamoto, J., Dasgupta, N.P., Matter, **2020**, *2*, 1025-1048.

[8] Zhang, H., Li, C., Piszcz, M., Coya, E., Rojo, T., Rodriguez-Martinez, L.M., Armand, M., Zhou, Z., Chem. Soc. Rev., **2017**, *46*, 797-815.

[9] Agarwal, R.C., Pandey, G.P., J. Phys. D: Appl. Phys., **2008**, *41*, 223001.

[10] Croce, F., Appetecchi, B., Persi, L., Scrosati, B., Nature **1998**, *394*, 456-458.

[11] Zhao, Q., Liu, X., Stalin, S., Khan, K., Archer, L.A., Nature Energy, **2019**, *4*, 365-373.

[12] Zheng, Q., Pesko, D.M., Savoie, B.M., Timachova, K., Hasan, A.L., Smith, M.C., Miller, III, T.F., Coates, G.W., Balsara, N.P., Macromolecules, **2018**, *51*, 2847-2858.

[13] Liu, T., Zhang, J., Han, W., Zhang, J., Ding, G., Dong, S., Cui, G., J. Electrochem. Soc., **2020**, *167*, 070527.

[14] Okada, M., Yamashita, Y., Ishii, Y., Makromolekul. Chem., **1964**, *80*, 196-207.

[15] Schaefer, J.L., Moganty, S.S., Yanga, D.A., Archer, L.A., J. Mater. Chem., **2011**, *21*, 10094.

[16] Yu, X., Manthiram, A., Energy Storage Mater., **2021**, *34*, 282-300.

[17] Commarieu, B., Paolella, A., Daigle, J.-C., Zaghib, K., **2018**, *9*, 56-63.

[18] Bockstaller, M.R., Mickiewicz, R.A., Thomas, E.L., Adv. Mater., **2005**, *17*, 1331–1349.

[19] Gilman, J.W., Kashiwagi, T., Lichtenhan, J.D., SAMPE J., **1997**, *33*, 40–46.

[20] Krishnamoorti, R., MRS Bull., **2007**, *32*, 341–347.

[21] Krishnamoorti, R., Vaia, R.A., Giannelis, E.P., Chem. Mater., **1996**, *8*, 1728–1734.

[22] Srivastava, S., Agarwal, P., Archer, L.A., Langmuir, **2012**, *28*, 6276-6281.

[23] Agarwal, P., Kim, S.A., Archer, L.A., Phys. Rev. Lett., **2012**, *109*, 258301.

[24] Kim, S.A., Archer, L.A., Macromolecules, **2014**, *47*, 687-694.

[25] Mangal, R., Nath, P., Tikekar, M., Archer, L.A., Langmuir, **2016**, *32*, 10621-10631.

[26] Ansari, S., Giannelis, E.P., J. Polym. Sci. B, **2009**, *47*, 888-897.

[27] Schmidt, D.F., Clement, F., Giannelis, E.P., Adv. Funct. Mater., **2006**, *16*, 417-425.

[28] Usuki, A., Kojima, Y., Kawasumi, M., Okada, A., Fukushima, Y., J. Mater. Res., **1993**, *8*, 1179-1184.

[29] Koerner, H., Price, G., Pearce, N.A., Vaia, R.A., Nat. Mater., **2004**, *3*, 115-120.

[30] Koerner, H., Liu, W.D., Alexander, M., Mirau, P., Dowty, H., Vaia, R.A., Polymer, **2005**, *46*, 4405-4420.

[31] Gilman, J.W., Kashiwagi, T., Lichtenhan, J.D., SAMPE J., **1997**, *33*, 40-46.

[32] Winey, K.I., Kashiwagi, T., Mu, M.F., MRS Bull., **2007**, *32*, 348-353.

[33] Mangal, R., Wen, Y.H., Choudury, S., Archer, L.A., Macromolecules, **2016**, *49*, 5202-5212.

[34] Liu, X., Abel, B.A., Zhao, Q., Li, S., Choudhury, S., Zheng, J., Archer, L.A., Macromolecules, **2019**, *52*, 8187-8196.

[35] Liu, X., Utomo, N.W., Zhao, Q., Zheng, J., Zhang, D., Archer, L.A., Macromolecules, **2021**, *54*, 426-439.

[36] Olabisi, O., Robeson, L., Shaw, M.T., Polymer-Polymer Miscibility, Academic Press: New York, **1969**.

[37] Vogel H., Phys. Z., **1921**, *22*, 645–646.

[38] Fulcher G.S., J. Amer. Ceram. Soc., **1925**, *8*, 339–355.

[39] Tammann G., Hesse W., Z. Anorg. Allg. Chem., **1926**, *156*, 245–257.

[40] Agrawal, A., Yu, H.-Y., Sagar, A., Choudhury, S., Archer, L.A., Macromolecules, **2016**, *49*, 8738-8747.

[41] Glatter, O., Kratky, O., Small Angle X-Ray Scattering; Academic Press: New York, **1982**.

[42] Yu, H.-Y., Srivastava, S., Archer, L. A., Koch, D. L., Soft Matter, **2014**, *10*, 9120−9135.

[43] Yu, H. Y., Koch, D. L., Langmuir, **2010**, *26*, 16801−16811.

[44] Choudhury, S., Agrawal, A., Wei, S., Jeng, E., Archer, L.A., Chem. Mater., **2016**, *28*, 2147-2157.

[45] Painter, P.C., Coleman, M.M., Essentials of Polymer Science and Engineering, Lancaster: DEStech Publications, Inc., **2009**.

[46] Hiemenz, P.C., Lodge, T.P., Polymer Chemistry, Boca Raton: CRC Press, **2007**, 2nd ed.

[47] Srivastava, S., Shin, J. H., Archer, L. A., Soft Matter, **2012**, *8*, 4097− 4108.

[48] Chremos, A., Douglas, J. F., Ann. Phys., **2017**, *529*, No. 1600342.

[49] Agrawal, A., Yu, H.-Y., Sagar, A., Choudhury, S., Archer, L.A., Macromolecules, **2016**, *49*, 8738-8747.

[50] Wang, M., Winter, H.H., Auernhammer, G.K., J. Colloid Interface Sci., **2014**, *413*, 159-166.

[51] Meng, Q., Heuzey, M.-C., Carreau, P.J., Polym. Degrad. Stab., **2012**, *97*, 2010-2020.

[52] Yang, Y., Kaufman, L.J., Biophys. J., **2009**, *96*, 1566-1585.

[53] Rubinstein, M., Colby, R.H., Polymer Physics, Oxford: Oxford University Press, **2003**.

[54] Strobl, G.R., The Physics of Polymers, Berlin: Springer, **1997**.

[55] Ferry, J.D., Viscoelastic Properties of Polymers, New York: John Wiley & Sons, Inc., **1961**.

[56] Wetton, R.E., Allen, G., Polymer, **1966**, *7*, 331-365.

[57] Sadej, M., Andrzejewska, E., Prog. Org. Coat., **2016**, *94*, 1-8.

[58] Lipatov, Y.S., Kosyanchuk, L.V., Nesterov, A.E., Antonenko, O., Polym. Int., **2003**, *52*, 664-669.

[59] Potoczek, M., Ceram. Int., **2006**, *32*, 739-744.

[60] Ito, K., J. Polym. Sci., **1975**, *13*, 401-413.

[61] Goto, A., Fukuda, T., Macromol., **1997**, *30*, 4272-4277.

[62] Mangal, R., Srivastava, S., Archer, L.A., Nat. Commun., **2015**, *6*, 1-9.

[63] Xiong, S., Xie, K., Diao, Y., Hong, X., Electrochim. Acta, **2012**, *83*, 78-86.

[64] Yu, X., Manthiram, A., Acc. Chem. Res., **2017**, *11*, 2653-2660.

[65] Zhao, Q., Liu, X., Zheng, J., Deng, Y., Warren, A., Zhang, Q., Archer, L.A., PNAS, **2020**, *117*, 26053-26060.

[66] Tudos, F., Foldes-Berezsnich, T., Prog. Polym. Sci., **1989**, *14*, 717-761.

[67] Yan, C., Yao, Y.-X., Chen, X., Cheng, X.-B., Zhang, X.-Q., Huang, J.-Q., Zhang, Q., Angew. Chem. Int. Ed., **2018**, *57*, 14055-14059.

[68] S. S. Zhang, Electrochim. Acta, **2012**, *70*, 344 –348.

[69] W.Li, H. Yao, K. Yan, G. Zheng, Z.Liang, Y.M.Chiang, Y. Cui, Nat. Commun., **2015**, *6*, 7436.

[70] H. Wu, Y. Cao, L. Geng, C.Wang, Chem. Mater., **2017**, *29*, 3572 – 3579.

[71] Van Der Voort, P., Gillis-D'Hamers, I., Vrancken, K.C., Vansant, E.F., J. Chem. Soc. Faraday Trans., **1991**, *87*, 3899-3905.

[72] Hair, M.L., J. Non-Crystalline Solids, **1975**, *19*, 299-309.

[73] Hair, M.L., Hertl, W., J. Phys. Chem., **1973**, *77*, 1965-1969.

[74] Sato, M., Kanbayashi, T., Kobayashi, N., Shima, Y., J. Catalysis, **1967**, *7*, 342-351.

[75] Allen J. Bard and Larry R. Faulkner, Electrochemical Methods: Fundamentals and Applications, New York: Wiley, **2001**, 2nd ed.

[76] Guo, J., Wen, Z., Wu, M., Jin, J., Liu, Y., Electrochem. Commun., **2015**, *51*, 59− 63.

[77] Zheng, J., Kim, M.S., Tu, Z., Choudhury, S., Tang, T., Archer, L.A., Chem. Soc. Rev., **2020**, *49*, 2701-2750.

[78] Wu, B., Lochala, J., Taverne, T., Xiao, J., Nano Energy, **2017**, *40*, 34–41.

[79] Chang, B.-Y., Park, S.-M., Annu. Rev. Anal. Chem., **2010**, *3*, 207-229.

[80] Manthiram, A., Fu, Y., Chung, S.-H., Zu, C., Su, Y.-S., Chem. Rev., **2014**, *114*, 11751-11787.

[81] Wei, S., Ma, L., Hendrickson, K.E., Tu, Z., Archer, L.A., J. Am. Chem. Soc., **2015**, *137*, 12143–12152.

[82] Li, T., Senesi, A.J., Lee, B., Chem. Rev., **2016**, *116*, 11128-11180.